Editors' Suggestion

Competing magnetic states in transition metal dichalcogenide moiré materials

Nai Chao Hu and Allan H. MacDonald
Department of Physics, The University of Texas at Austin, Austin, Texas 78712, USA

(Received 1 September 2021; revised 18 November 2021; accepted 19 November 2021; published 3 December 2021)

Small-twist-angle transition metal dichalcogenide (TMD) heterobilayers develop isolated flat moiré bands that are approximately described by triangular lattice generalized Hubbard models [F. Wu, T. Lovorn, E. Tutuc, and A. H. MacDonald, Phys. Rev. Lett. **121**, 026402 (2018)]. In this paper we explore the metallic and insulating states that appear under different control conditions at a density of one electron per moiré period and the transitions between them. By combining fully self-consistent Hartree-Fock theory calculations with strong-coupling expansions around the atomic limit, we identify four different magnetic states and one nonmagnetic state near the model phase diagram's metal-insulator phase transition line. Ferromagnetic insulating states, stabilized by nonlocal direct exchange interactions, are surprisingly prominent.

DOI: 10.1103/PhysRevB.104.214403

I. INTRODUCTION

Moiré materials, formed by stacking layered two-dimensional (2D) van der Waals semiconductors or semimetals with small differences in lattice constant or orientation, have attracted attention recently as a highly tunable platform to study strong correlation phenomena. The low-energy physics of a moiré material is accurately described by an emergent periodic Hamiltonian [1–3] that is insensitive to commensurability between the moiré pattern and the underlying lattice. Stimulated by the recent experimental realization [4–6] of magic angle physics in twisted bilayer graphene, experimental attention has expanded to include other graphene-based multilayers with twists [7–14] and also twisted transition metal dichalcogenide (TMD) bilayers [15–25]. The valence bands of TMD heterobilayers and Γ-valley homobilayers [26] are described by emergent models in which interacting spin-1/2 electrons experience an external potential with triangular lattice periodicity and therefore map directly to models of electrons on triangular or honeycomb lattices. This paper is devoted to a study of the properties of triangular lattice moiré materials and focuses on the case of one hole per moiré period, in which correlations are strongest. We examine the crossover from the narrow-band regime at small twist angles, where the system maps to a one-band Hubbard model with dominant on-site interactions, to the regime closer to the metal-insulator phase transition, where important differences appear.

Our discussion is based mainly on a mean-field Hartree-Fock approximation used to address the interplay between periodic modulation and Coulomb interactions that control the hybridization between orbitals centered on different sites and therefore exchange interactions of spins on the system's triangular lattice. Because it is a mean-field approach, the Hartree-Fock approximation cannot account for dynamic fluctuations in spin configuration but can accurately describe the energy of particular spin configurations. Importantly for the present application, the Hartree-Fock approximation has the advantage over spin density functional theory [27] that it correctly accounts for the absence of self-interaction [28] when electrons are localized near lattice sites. We expect the Hartree-Fock approximation to overestimate the stability of insulating states relative to metallic states. (Indeed, this expectation is confirmed by comparison with separate exact-diagonalization calculations for the same model [29].) Our calculations can therefore provide a lower bound on the moiré modulation strength that drives the system from a metallic to an insulating state at a given interaction strength. Unlike exact-diagonalization calculations, Hartree-Fock calculations can be accurately converged with respect to system size.

Our goal in this paper is to identify differences between moiré material physics and single-band Hubbard model physics, with particular emphasis on the prospects for tuning the system into exotic spin liquid states. Figure 1 shows the phase diagram in a space defined by dimensionless modulation strength $\alpha^2(V_M, \phi, a_M)$ and interaction strength $r_s^*(\epsilon, a_M)$ parameters. The full phase space of the problem is actually three-dimensional since the phase ϕ (see below) of the moiré potential Fourier amplitude also plays a role. (a_M is the moiré material lattice constant.) The lowest-energy hole band is spectrally isolated for $\alpha \lesssim 0.1$, the range covered in Fig. 1, unless ϕ is very close to a honeycomb value (see below). We find that the three-sublattice antiferromagnetism expected [30] in the insulating state transforms to stripe magnetism and finally to ferromagnetism with increasing r_s^* and that a semimetallic state with three-sublattice order occurs on the metallic side of the metal-insulator phase transition. The transition to ferromagnetic insulating states at strong interactions opens up new opportunities to engineer strongly frustrated quantum magnetism. Given the possibility of *in situ* tuning between different spin states, these findings demonstrate that moiré materials are an exceptionally promising new system for the exploration of two-dimensional quantum magnetism.

The rest of this paper is organized as follows: In Sec. II we review the moiré material model, discuss expected properties, and introduce the mean-field formalism. In Sec. III,

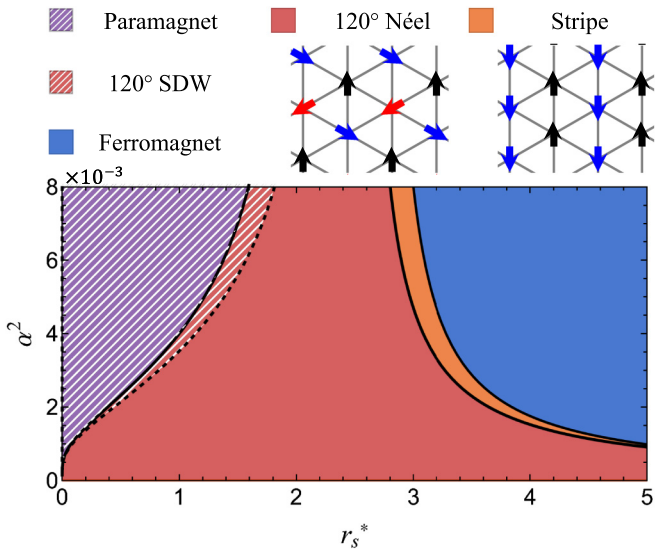

FIG. 1. Hartree-Fock phase diagram for triangular lattice moiré materials with one hole per unit cell. The two dimensionless control parameters (see the text) are the interaction strength r_s^* and α^2, a parameter that is inversely related to the moiré potential strength. First-order and second-order phase transitions are marked by solid and dashed black lines, respectively. States close to the top left corner of the phase diagram (hashed) are metallic. States at the bottom right of the phase diagram are insulating. A narrow semimetallic state (labeled SDW, spin density wave) that shares spatial symmetries with the three-sublattice noncollinear insulating state hugs the metallic side of the metal-insulator transition. An unexpected phase transition into an insulating ferromagnetic (blue) state at strong interaction strengths is interrupted by a narrow collinear antiferromagnetic stripe state (orange). This phase diagram was calculated for the moiré modulation phase (see the text) $\phi = 26^\circ$. The lines follow approximate phase boundary expressions explained in the text.

we discuss our results for spin interactions in insulating moiré materials. We comment specifically on the necessary conditions for nonzero Hall conductance, concluding that although nontrivial band topology is unlikely, applying a magnetic field might induce a nonzero Hall conductance in doped insulators. Finally, in Sec. IV we summarize our results and highlight important directions for future research.

II. INTERACTING CONTINUUM MODEL

The low-energy physics of TMD moiré materials, like that of twisted bilayer graphene, is most conveniently captured by a continuum model [1]. Since TMDs are generally good insulators with strong spin-orbit coupling from the transition metal atoms, only the topmost valence band needs to be included in the low-energy model, yielding one state for each valley. Because of spin-valley locking, we can equivalently choose to identify these states by their spins or by their valleys. The type-II band alignment of TMD heterojunctions means that only one layer is active at low energy. Hence, the fermion field operators $\psi_\alpha^{(\dagger)}(\mathbf{r})$ in this model carry only one label, representing locked spin/valley, while the effect of the other layer is integrated out, appearing only as a contribution to the moiré potential $\Delta(\boldsymbol{r})$ [1,31]. When the Fourier expansion of Δ is truncated at the first shell of moiré reciprocal lattice vectors $\mathbf{b}_j$,

$$\Delta(\mathbf{r}) = \sum_{j=1}^{6} V_j \exp\left[i\mathbf{b}_j \cdot \mathbf{r}\right], \tag{1}$$

where $V_j = V_M \exp[(-1)^{j-1} i\phi]$. V_j and ϕ are material-dependent parameters, with V_M characterizing the moiré modulation strength and ϕ being its shape. The single-particle Hamiltonian of the moiré continuum model

$$H_0 = T + \Delta(\mathbf{r}), \tag{2}$$

where T is the single-particle kinetic energy operator for electrons with effective mass m^*, is spin independent. In a plane-wave representation

$$H_{0\mathbf{b},\mathbf{b}'}(\mathbf{k}) = -\frac{\hbar^2}{2m^*}(\mathbf{k}+\mathbf{b})^2\,\delta_{\mathbf{b},\mathbf{b}'} + \sum_{j=1}^{6} V_j \delta_{\mathbf{b}_j,\mathbf{b}-\mathbf{b}'}, \tag{3}$$

where momentum $\mathbf{k}$ is in the first moiré Brillouin zone and $\mathbf{b}$ are moiré reciprocal lattice vectors.

The key feature of this single-particle model, as pointed out in Ref. [1], is that the lowest-energy hole band is isolated and has a bandwidth W that decreases exponentially with moiré period a_M. One physical intuition for this behavior is based on the observation that the model can be approximated, in the large-a_M limit, as a lattice of weakly coupled harmonically confined electrons. Ignoring the "remote-band" holes for the moment, we can readily see that the largest effect of Coulomb interactions is to impose an energy penalty U on doubly occupied sites, which is the essence of Hubbard model physics. But in contrast to the simplest nearest-neighbor Hubbard model, the ratio of the second-nearest-neighbor hopping to the nearest-neighbor hopping can be increased by decreasing the modulation strength, a property easily explained in the harmonic oscillator approximation, increasing the magnetic frustration of insulating states.

In addition to allowing flexible tuning of U/W, the sublattice content of the hexagonal Bravais lattice on which the model sits can be controlled. The symmetry of the moiré potential can be changed from that of a triangular lattice to that of a honeycomb lattice, with perfect honeycomb behavior achieved at $\phi = 60^\circ$, $\phi = 180^\circ$, and $\phi = -60^\circ$. The applicable value of ϕ can be adjusted experimentally by choosing different TMD heterojunctions [27,29]. Over a finite range of ϕ near the honeycomb values, the moiré potential has local minima at the honeycomb lattice sites. When ϕ is close to one of the honeycomb values, the potential minima at the two honeycomb sublattices differ slightly in value, allowing inversion-symmetry-breaking sublattice-mass terms to be added to the Hamiltonian when expressed in terms of its tight-binding model limit. Here we focus on triangular lattice Hubbard model Mott physics by restricting our attention to the case of one electron per triangular lattice unit cell. At this density the second minimum plays a role only over narrow ranges of ϕ by increasing the spread of the ground state Wannier wave function and slightly altering the competition between different states.

The many-body Hamiltonian in TMD moiré materials has three terms: the kinetic energy, the moiré modulation

potential, and the Coulomb interaction term. It follows that the many-body physics depends, up to an energy scale, on ϕ and on two dimensionless parameters. We choose to describe the phase diagram in terms of the standard electron gas interaction strength parameter,

$$r_s^* = \frac{1}{\sqrt{\pi n} a_B^*} = \left(\frac{3}{4\pi^2}\right)^{1/4} \frac{V_C^s}{T^s} = \left(\frac{3}{4\pi^2}\right)^{1/4} \frac{a_M}{a_B} \frac{m^*}{m} \frac{1}{\epsilon}, \tag{4}$$

and a second parameter that characterizes the ratio of the single-particle Wannier function spread to the moiré period. Here we have defined two energy scales, the kinetic energy scale at the moiré length $T^s = \hbar^2/2m^* a_M^2$ and the Coulomb interaction at the moiré length $V_C^s = e^2/2\epsilon a_M$, and one length scale, the Bohr radius $a_B^* \equiv \hbar^2\epsilon/e^2 m^*$. Our interaction strength parameter r_s^* can be viewed as the typical distance between electrons in Bohr radius units. The definition of the second dimensionless parameter is motivated by the small-twist-angle limit in which the lowest-energy flat band's Wannier function is accurately approximated by the Gaussian ground state of the harmonic potential $m^*\omega^2 \mathbf{r}^2/2$ obtained by expanding the moiré modulation potential around a minimum. It follows from this expansion that $\omega^2 = \beta V_M/m^* a_M^2$, where $\beta = 16\pi^2 \cos(\phi + k120^\circ)$, with k being an integer chosen to place the argument of the cosine function $\in (-60^\circ, 60^\circ)$ [32]. We choose

$$\alpha \equiv \frac{a_W^2}{a_M^2} = \frac{\hbar}{\sqrt{m^* \beta V_M a_M^2}}, \tag{5}$$

where $a_W^2 = \hbar/m^*\omega$ is the square of the oscillator length scale, as the second dimensionless interaction parameter. Notice that α is dependent on both the phase ϕ and the magnitude V_M of the moiré potential. In Fig. 1 the phase diagram is plotted in terms of r_s^* and α^2, with the latter variable chosen to simplify its dependence on V_M. Choosing α to be a dimensionless model parameter eliminates most of the phase diagram's dependence on ϕ, with exceptions applying very close to $\phi \sim 60^\circ + k120^\circ$ and deep in the metallic state.

A. Symmetries

For later convenience, we briefly summarize the symmetries of the problem. The model has a full SU(2) rotation symmetry of the locked spin/valley degree of freedom and C_{3v} orbital symmetry; the D_{3h} symmetry of a TMD monolayer is reduced by stacking. The nontrivial operations of C_{3v} are rotations by $2\pi/3$,

$$C_3 : \psi_\alpha(\mathbf{x}) \to \psi_\alpha(R_{2\pi/3}\mathbf{x}), \tag{6}$$

and the mirror operation M_y,

$$M_y : \psi_\alpha(x, y) \to \psi_\alpha(x, -y). \tag{7}$$

In the absence of a magnetic field, the model is invariant under time reversal, which switches the spins:

$$\mathcal{T} : \psi_\alpha(\mathbf{x}) \to i(\sigma^y)_{\alpha\beta}\, \psi_\beta(\mathbf{x}), \tag{8}$$

where σ^y is the Pauli matrix and acts in spin space. We note that two spins are interchanged by only time-reversal symmetry (TRS):

$$H^{\downarrow}_{\mathbf{b},\mathbf{b}'}(\mathbf{k}) = H^{\uparrow *}_{-\mathbf{b},-\mathbf{b}'}(-\mathbf{k}), \tag{9}$$

where we make use again of the discrete translational invariance of our moiré system. At this level of approximation, each spin-projected Hamiltonian itself also satisfies a spinless TRS property:

$$H^{\uparrow/\downarrow}_{\mathbf{b},\mathbf{b}'}(\mathbf{k}) = H^{\uparrow/\downarrow *}_{-\mathbf{b},-\mathbf{b}'}(-\mathbf{k}). \tag{10}$$

We also note that since inversion symmetry is broken in TMD monolayers, unlike in twisted bilayer graphene, Berry curvature is not required to vanish identically throughout the moiré Brillouin zone.

B. Weak and strong modulation limits

Before carrying out detailed self-consistent Hartree-Fock calculations, we provide some orientation by discussing some simple limits in which electronic properties are well understood. We first consider the weak-modulation limit, where bandwidths are large and moiré bands overlap, which should give rise to behavior close to that of the 2D homogeneous electron gas (jellium) model. It is well known that Hartree-Fock approximation fails badly for magnetic properties by predicting that 2D jellium is ferromagnetic above a small value of $r_s \simeq 2.01$, whereas quantum Monte Carlo calculations [33,34] show that the paramagnetic fluid remains stable up to a much larger interaction strength $r_s \sim 25.56$. In the opposite strong-modulation limit electrons occupy Wannier functions centered on potential minima. At one electron per moiré period, strong on-site Coulomb interactions leave only spin degrees of freedom at low energies. Because electronic correlations are less subtle in this limit, the Hartree-Fock approximation predicts magnetic states much more reliably, and we can fit ground state energies to determine the parameters of spin Hamiltonians. The only quadratic spin Hamiltonian that satisfies all the symmetry requirements of our model is the isotropic Heisenberg model:

$$H_{\text{spin}} = J_1 \sum_{\langle i,j\rangle} \mathbf{S}_i \cdot \mathbf{S}_j + J_2 \sum_{\langle\langle i,j\rangle\rangle} \mathbf{S}_i \cdot \mathbf{S}_j, \tag{11}$$

where $\langle i, j\rangle$ and $\langle\langle i, j\rangle\rangle$ label nearest-neighbor and next-nearest-neighbor interactions. In the case of $J_1 > 0$, the classical-spin triangular lattice ground state is the 120° Néel state for $J_2/J_1 < 1/8$ and a stripe state for $1/8 < J_2/J_1 < 1$ [30]. It is widely believed that quantum fluctuations play a vital role in determining the phase near $J_2/J_1 = 1/8$, although extensive numerical efforts over the years [35–40] have not reached a clear consensus on the nature of the potentially exotic phase. When the strong modulation Hamiltonian is approximated by a Hubbard model, both interactions are antiferromagnetic [41], with $J_2/J_1 \ll 1$, except possibly very close to the metal-insulator phase transition. In the present system, however, we find that insulating states are ferromagnetic at large r_s^* and interpret this property as evidence for beyond Hubbard model physics. The band topology of the ferromagnetic state obviously has zero Chern number since spin-projected bands are then time reversal invariant. The

topology of the 120° Néel is less obvious since ↑ and ↓ band states are mixed by the noncollinear spin structure. We nevertheless find that they are topologically trivial, as we show in Sec. III. For extremely localized electrons ($\alpha \to 0$), all magnetic configurations will become degenerate.

C. Self-consistent Hartree-Fock approximation

Our main goals in this paper are to gain insight into the spin physics of the moiré superlattice Mott insulator phase and to obtain a rough estimate of the boundary between insulating and metallic states. As long as the spin ground state is close to its classical limit, that is to say, as long as fluctuations in the spin direction in the magnetic ground state are not extremely large, the Hartree-Fock approximation is normally accurate. One important advantage of the Hartree-Fock approximation is that it completely removes spurious self-interaction effects in the limit that the electrons are reasonably strongly localized around their moiré lattice sites. As the twist angle is increased and the moiré pattern's lattice constant is reduced, two-dimensional spin density functional theory [27], which has much the same structure as Hartree-Fock theory, becomes an attractive alternative. Even when quantum spin fluctuations in the insulating ground state are large, either approach can be used to approximate the classical energy function of the spin subsystem, and quantum corrections can be calculated using standard spin-wave techniques.

The Hartree-Fock energy functional is the expectation value of the many-electron Hamiltonian in a single Slater determinant ground state. Minimizing the energy functional with respect to single-particle wave functions yields a mean-field Hamiltonian that adds an interaction self-energy $\Sigma^{\rm HF}$ to the single-particle Hamiltonian which can be expressed in terms of the single-particle density matrix $\rho = \sum_n |\psi_n\rangle\langle\psi_n|$, where the sum is over occupied moiré-band Bloch wave functions. The mean-field electronic structure of moiré superlattices is best evaluated using a plane-wave representation in which the Hartree-Fock self-energy $\Sigma^{\rm HF}$ at each $\mathbf{k}$ in the Brillouin zone is a matrix in reciprocal lattice vectors $\mathbf{b}$:

$$\Sigma^{\rm HF}_{\alpha,\mathbf{b};\beta,\mathbf{b}'}(\mathbf{k}) = \frac{\delta_{\alpha,\beta}}{A}\sum_{\alpha'} V_{\alpha'\alpha}(\mathbf{b}'-\mathbf{b})\sum_{\mathbf{k}',\mathbf{b}''}\rho_{\alpha',\mathbf{b}+\mathbf{b}'';\alpha',\mathbf{b}'+\mathbf{b}''}(\mathbf{k}') - \frac{1}{A}\sum_{\mathbf{b}'',\mathbf{k}'} V_{\alpha\beta}(\mathbf{b}''+\mathbf{k}'-\mathbf{k})\rho_{\alpha,\mathbf{b}+\mathbf{b}'';\beta,\mathbf{b}'+\mathbf{b}''}(\mathbf{k}'). \tag{12}$$

In Eq. (12) Greek letters label spin, A is the finite sample area corresponding to a discrete Brillouin zone mesh, and $\rho_{\alpha,\mathbf{b};\beta,\mathbf{b}'}$ is the self-consistently determined momentum-space density matrix. Starting with a physically plausible density matrix ρ_0, we minimize the energy by performing self-consistent iterations. Because the many-body interaction is invariant under both translations and spin rotations, if we start from a density matrix ρ_0 which satisfies a symmetry $\hat{O}$ of H_0 ($[\rho_0, \hat{O}] = 0$, $[H_0, \hat{O}] = 0$), then the symmetry survives under iteration. That is to say, $H^{\rm HF}$ commutes with $\hat{O}$ at every iteration step. In many cases the minimum-energy Hartree-Fock state breaks symmetries of H_0, and these solutions are found under iteration only by starting with a broken-symmetry density matrix. As argued in Sec. II B, the phase diagram contains paramagnetic states that do not break any symmetries, ferromagnetic states with spontaneous collinear spin polarization that do not break lattice translational symmetries, stripe states with collinear order and a doubled unit cell area, and 120° Néel states with both a tripled unit cell area and noncollinear spin order. We obtain solutions of the first two kinds by appropriate choices of the initial density ρ_0. Each possible type of reduced translational symmetry implies a different reciprocal lattice and therefore has to be encoded explicitly in the reciprocal lattice employed and considered separately. Solutions can be classified as insulating with a gap between occupied and empty states or metallic with Fermi surfaces in the Brillouin zone on which occupation numbers change. At one electron per moiré period, the paramagnetic state must be metallic, but all other states we consider can be insulating. We show typical Hartree-Fock self-consistent band structures for insulating and metallic magnetic ordered states in Fig. 2.

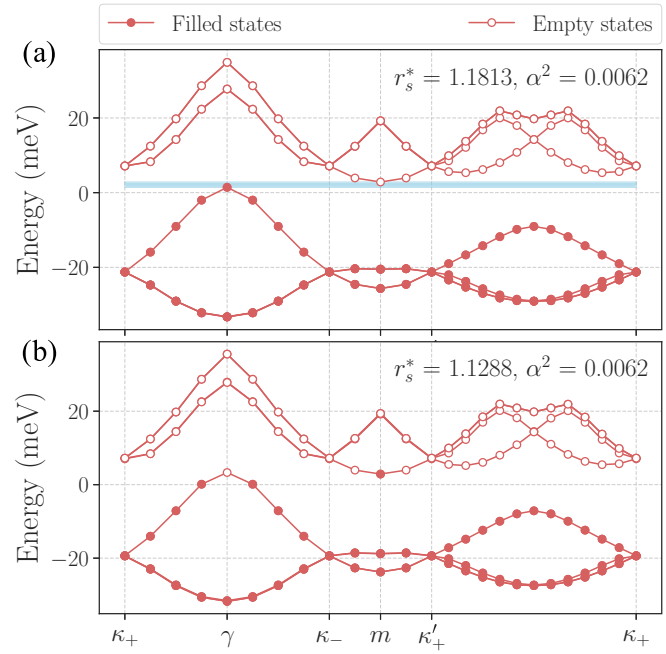

FIG. 2. Typical Hartree-Fock band structures for three-sublattice magnetic states. (a) The 120° Néel insulator. The energy gap, indicated by the light-blue band, is small because the state is close to the metal-insulator phase transition. (b) At smaller r_s^*, we obtain a 120° semimetallic SDW state. (See Appendix A for further details on model parameters.)

III. RESULTS

Having introduced the problem, we now present the predictions of Hartree-Fock theory for the phase diagram. We focus first on a fixed moiré modulation phase $\phi = 26°$, estimated [1] to apply to the $WSe_2/MoSe_2$ heterobilayer system. (As emphasized earlier, we have chosen the dimensionless parameters used to construct the phase diagrams with a view toward minimizing any dependence on ϕ.). We have performed self-consistent Hartree-Fock calculations on a discrete two-dimensional grid of system parameters. The phase diagram in Fig. 1 was constructed by interpolating between

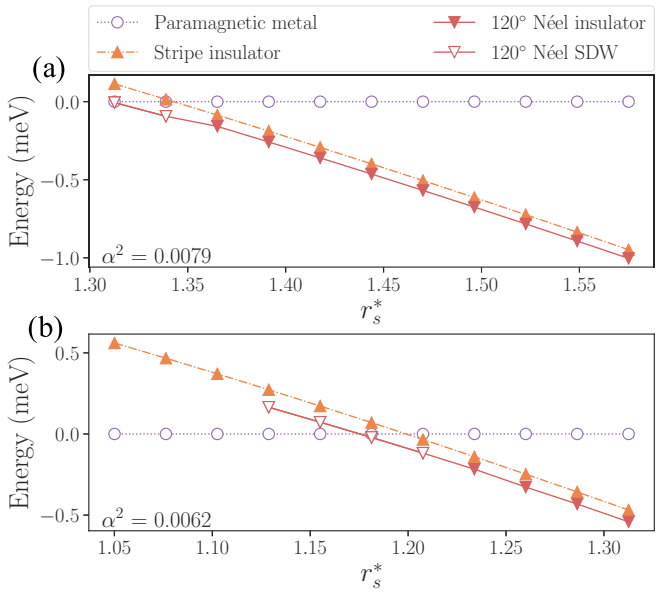

FIG. 3. Phase competition near the metal-insulator transition. We choose two values of the Wannier localization parameter α^2 to closely examine the emergence of the 120° semimetallic SDW state and the disappearance of metallic states with increasing r_s^*. Energies are plotted relative to the nonmagnetic metallic state energy. The ferromagnetic state has higher energy than both antiferromagnetic structures and is hence omitted in these plots. At the relatively large α^2 values we choose, the lowest-energy state clearly changes from a paramagnetic metal to a 120° semimetallic SDW and then to a 120° antiferromagnetic insulator.

this discrete set of results; a pixelated summary of our actual calculation results is presented in Fig. 7 in Appendix A. The influence of ϕ on the phase diagram will be discussed later.

Each solution of the Hartree-Fock equations corresponds either to a local minimum of the energy functional or to a saddle point at which energy can be reduced by breaking symmetries. We have identified the ground state by comparing the total energies of all solutions. Translational symmetry is allowed to break down to only either the two-sublattice (stripe) state or the three-sublattice (120°) state, both of which are common in triangular lattice phase diagrams. In our calculations, all phase transitions that change translational symmetry are of the first order, and all that do not are continuous.

Two sets of two phase boundaries are of particular interest: metal-insulator transitions on the left-hand side of Fig. 1 and magnetic transitions within the insulating state on the right-hand side. We see in Fig. 1 that the competition near the metal-insulator phase transition is mostly between a nonmagnetic metallic state and the noncollinear three-sublattice state. When we examine the region near the metal-insulator phase transition closely, however, we find that the three-sublattice insulator becomes a semimetal at a critical r_s^* that is slightly larger than the critical r_s^* at which the magnetic order disappears (see Fig. 3). As a result, itinerant magnets with the same magnetic structure as that of the noncollinear three-sublattice insulating state appears near the metal-insulator transition. Thus, within the Hartree-Fock approximation, the insulator-to-metal transition is a continuous phase transition but is closely followed by a first-order transition to a nonmagnetic metallic state. We associate the increasing stability of 120° semimetallic spin density wave (SDW) states, relative to 120° insulating states at larger values of α, with increased itinerancy and associated larger values of t_2/t_1. We also find that close to the metal-insulator phase boundary, the stripe and 120° insulating states have very similar energy densities, although the stripe order energies are always slightly larger.

To gain some analytic insight into the form of this phase boundary, we make an approximation that is accurate in the small-twist-angle limit discussed earlier. We estimate the nearest-neighbor hopping parameter by using harmonic oscillator wave functions, which yields

$$t_1 = \frac{\hbar^2}{2m^* a_M^2}\left(\frac{1}{4\alpha^2} - \frac{1}{\alpha}\right)\exp\left(-\frac{1}{4\alpha}\right). \tag{13}$$

The nonmonotonic dependence of t_1 on α is related to a breakdown of the assumption of strongly localized Wannier orbitals at small α. To simplify the approximate phase boundary expression we derive below, we measure energies in units of the moiré kinetic energy scale T^s and write $\tilde{X} \equiv X/T^s$. On physical grounds, the metal-insulator transition should occur at a critical value of the ratio $c = U/t_1$. Since the ratio of the moiré lattice constant to the Wannier function width, which is $\propto \theta^{1/2}$, changes slowly in the parameter range of interest, this criterion corresponds approximately to a critical c' of the ratio V_C^s/t_1, which is proportional to r_s^* [see Eq. (4)]. In estimating the phase boundary line we ignore the $1/\alpha$ factor in Eq. (13) since α is small. This yields $\alpha^2 = [8W_{-1}(-\sqrt{\tilde{t}_1}/4)]^{-2}$, where $W_{-1}(x)$ is the Lambert W function and the branch is chosen by the monotonic property of t_1. The Hartree-Fock metal-insulator phase boundary closely follows the $c' = 1.9$ line in the phase diagram, which corresponds to $c = 2c'/\sqrt{\alpha} \sim 15.1$. Given this value for c, we can estimate that the magnetic ordering energy on the insulating side of the phase diagram $4t_1^2/U$ is ∼4.0 meV for experimental systems with moiré period $a_M \sim 5$ nm [23,24], which compares well with the experimental estimate of $J_1 \sim 3$ meV [23].

We now turn to the magnetic transitions that occur within the insulating region in the phase diagram. We find that the insulators are ferromagnetic at large r_s^* and that all magnetic states are very close in energy near the 120° state to ferromagnet phase boundary. Evidently, this phase boundary is associated with a change in sign of the dominant near-neighbor interactions between spins, leaving all states close in energy. The energies of competing states close to this phase boundary are plotted in Fig. 4, where we see that the ferromagnetic state is strongly favored at large interaction strength r_s^*, that the stripe phase is stable over a narrow range of r_s^* between the 120° and ferromagnetic states, and that the stripe state stability range broadens at larger α.

To understand these observations, we consider interactions within the spin-only Hilbert space discussed in Sec. II B. Assuming the spin Hilbert space is correctly described by the J_1-J_2 spin model of Eq. (11), the classical energies of the

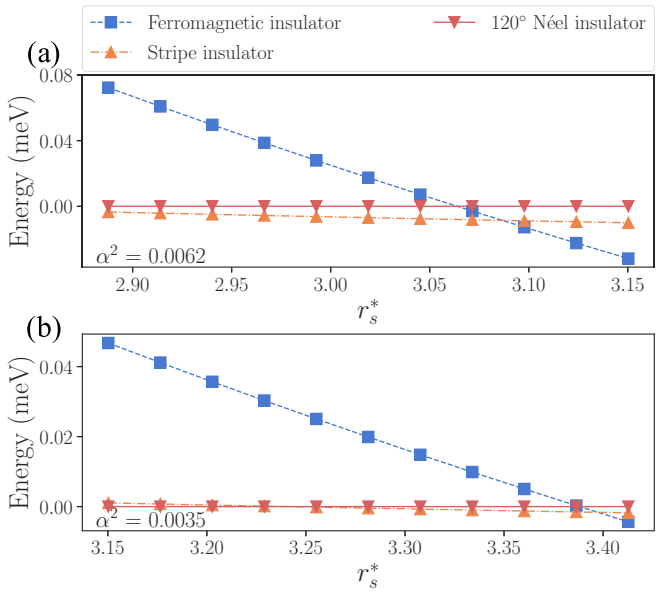

FIG. 4. Phase competition near the antiferromagnet-ferromagnet transition. Again, the Wannier localization parameter α^2 is fixed, and interaction strength r_s^* is varied. Energies are plotted relative to the 120° Néel insulators. Paramagnetic metals in this case have much higher energy than any insulators and therefore are omitted. The lowest-energy state changes from a 120° antiferromagnetic insulator at small r_s^* to a stripe insulator and then to a ferromagnetic insulator at large r_s^*. The stripe phase becomes more stable at larger α.

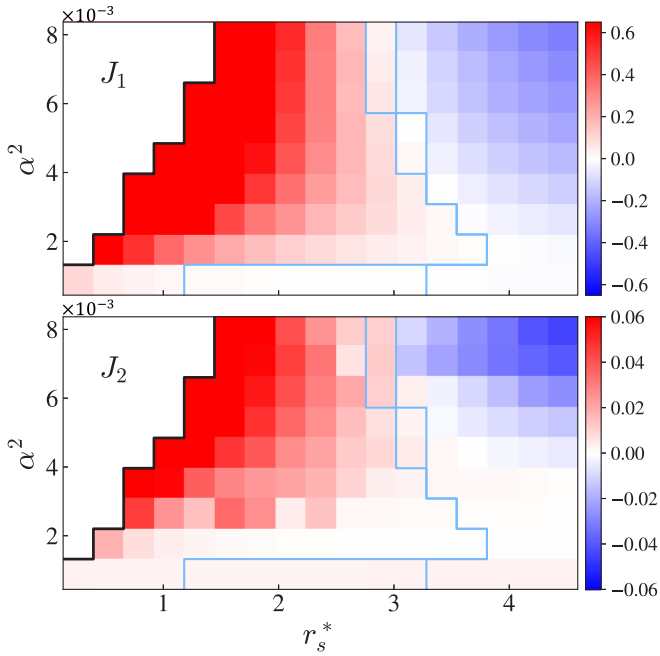

FIG. 5. Values of J_1 and J_2 (in meV) for a fixed a_M throughout the phase diagram, obtained by fitting ground-state energies of different insulating magnetic orders to a J_1-J_2 Heisenberg model [see Eqs. (17) and (18)]. We observe that J_1 changes sign at the antiferromagnet-ferromagnet phase boundary, while J_2 changes sign inside the region of ferromagnetic states.

ferromagnetic, stripe, and 120° states are

$$e_1 = \frac{1}{4N}(3NJ_1 + 3NJ_2) = \frac{3}{4}J_1 + \frac{3}{4}J_2, \tag{14}$$

$$e_2 = \frac{1}{4N}(-NJ_1 - NJ_2) = -\frac{1}{4}J_1 - \frac{1}{4}J_2, \tag{15}$$

$$e_3 = \frac{1}{4N}(-3NJ_1/2 + 3NJ_2) = -\frac{3}{8}J_1 + \frac{3}{4}J_2. \tag{16}$$

It follows that we can determine numerical values for the coupling constants from the energy differences between the three magnetic states we consider in our Hartree-Fock calculations:

$$J_1 = \tfrac{8}{9}(e_1 - e_3), \tag{17}$$

$$J_2 = e_1 - e_2 - J_1. \tag{18}$$

We plot the J_1 and J_2 values obtained in this way in Fig. 5, where we see that the signs of J_1 and J_2 are strongly correlated and that the ferromagnetic state phase boundary aligns with the line on which J_1 changes sign.

One of the most intriguing aspects of our results is the appearance (at the mean-field level) of a stripe state. This finding suggests that these moiré materials may provide a clean realization of the long-sought J_1-J_2 quantum spin liquid state, which is born out of the quantum fluctuations near the boundary between the three-sublattice state and the stripe state. However, we caution the readers that our system is not fully equivalent to a J_1-J_2 model. In the case of an exact J_1-J_2 Heisenberg model, stripe states appear for $J_2/J_1 \gtrsim 1/8$. Since we estimate values of the exchange couplings by comparing energies of a small number of magnetic configurations, our results do not rule out other possibilities, one example of which is that the third-nearest-neighbor exchange coupling J_3 is ferromagnetic and $-J_3/J_1 \gtrsim 1/9$. Since current experimental studies operate in parameter ranges close to the metal-insulator transition, they may need to be tuned to larger r_s^* to reach the ferromagnetic state, for example, by choosing materials with smaller lattice mismatches or tuning twist angles.

The J_1 sign change is associated with interactions that are nonlocal in the model's Wannier function lattice representation [42] and are therefore absent in generalized Hubbard-model interaction approximations. For a given pair of near-neighbor sites the nonlocal interaction terms can be characterized as either an interaction-assisted hopping term,

$$V_{ah} = \sum_{\sigma} \langle 2\sigma, 1\bar{\sigma}|V_C|1\sigma, 1\bar{\sigma}\rangle\, c^\dagger_{2\sigma} c^\dagger_{1\bar{\sigma}} c_{1\bar{\sigma}} c_{1\sigma}, \tag{19}$$

or an intersite-exchange term,

$$V_x = \sum_{\sigma_1,\sigma_2} \langle 2\sigma_1, 1\sigma_2|V_C|1\sigma_1, 2\sigma_2\rangle\, c^\dagger_{2\sigma_1} c^\dagger_{1\sigma_2} c_{2\sigma_2} c_{1\sigma_1}, \tag{20}$$

where σ is a spin label and $\bar{\sigma} = -\sigma$. At half filling, V_{ah} is physically equivalent to hopping, so its main effect is to enhance the antiferromagnetic coupling constant. On the other hand, V_x, being an exchange term, carries a minus sign from fermionic ordering and therefore favors ferromagnetic coupling [43]. We now argue the transition happens when the enhanced antiferromagnetic coupling $4(-t_1 + |V_{ah}|)^2/U$ is equal to $2|V_x|$ in magnitude. We assume we are in the strongly interacting regime, where $V_{ah/x} \sim t_1^2/U \ll t_1$. This

allows us to compare the simplified antiferromagnetic energy scale $4t_1^2/U$ to the ferromagnetic energy scale,

$$2|V_x(\mathbf{1},\mathbf{2};\mathbf{2},\mathbf{1})| = 2U\exp\left(-\frac{1}{2\alpha}\right), \tag{21}$$

where **1** and **2** are nearest neighbors. We again ignore the $1/\alpha$ factor in the expression of t_1 in Eq. (13) to the lowest order. It is clear that the antiferromagnet-ferromagnet phase boundary should be described by $1/2\sqrt{2}\alpha^2 = \tilde{U}$, i.e., $\alpha^2 = 1/2\sqrt{2}\tilde{U} \sim 1/r_s^*$ [44], which agrees well with our Hartree-Fock approximation.

To explicitly explore the influence of ϕ on the phase boundaries that remains for our choice of dimensionless interaction parameters, we carry out self-consistent Hartree-Fock calculations vs ϕ at two points in our r_s^*-α^2 phase diagram (Fig. 1) that lie just to the right of the two phase transition boundaries. In order to describe how the generic triangular lattice smoothly evolves into a honeycomb lattice we consider the range from $\phi = 30^\circ$ to $\phi = 60^\circ$ at which the additional honeycomb lattice symmetries become exact. Because we study the case of one electron per triangular lattice unit cell, the electron density is half of that associated with honeycomb lattice Mott insulator states. As ϕ approaches 60°, the two local potential minima in the moiré unit call become more nearly-equivalent, and inversion symmetry relative to the midpoint between the two minima is more nearly-established. In our self-consistent Hartree-Fock calculations we find that at the density we study this approximate symmetry is always strongly broken. Even at $\phi = 60^\circ$, the electrons tend to occupy only one honeycomb sublattice, as we verify by explicit calculation, and the role of the difference between ϕ and 60° acts as a weak symmetry-breaking parameter. At no point in this evolution do the lowest two self-consistent Hartree-Fock bands overlap and develop the Dirac points of single-orbital honeycomb lattice bands. The broken symmetry lowers energies by increasing separations between electrons. In the language of the honeycomb lattice Hubbard model, occupying only one honeycomb sublattice avoids the near-neighbor electron-electron interaction term in the Hamiltonian with coupling constant U_1.

From the arguments in Sec. II, we anticipate the physical effect of changing a triangular lattice to a honeycomb lattice is (approximately) equivalent to increasing the effective Wannier function width α. For this reason we expect the metal-insulator phase boundary to move toward larger r_s^* as $\phi \to 60^\circ$, while the antiferromagnet-ferromagnet transition boundary moves toward smaller r_s^*. For a r_s^*-α^2 point on the insulating side of the metal-insulator phase boundary, we show in Fig. 6(a) that the lowest-energy state changes from a noncollinear magnetic insulator to a 120° semimetallic SDW and finally to a paramagnetic metal as $\phi \to 60^\circ$. In contrast, in Fig. 6(b), no phase transition is observed. The ferromagnetic ground state becomes more and more stable as the antiferromagnet-ferromagnet phase boundary moves toward smaller r_s^*.

Last but not least, we examine the possibility of nontrivial band topology in the magnetically ordered states. For ferromagnetic and stripe states, it is straightforward to show that the spin-projected orbital Hamiltonians are time reversal invariant. These states therefore cannot have nonzero Chern

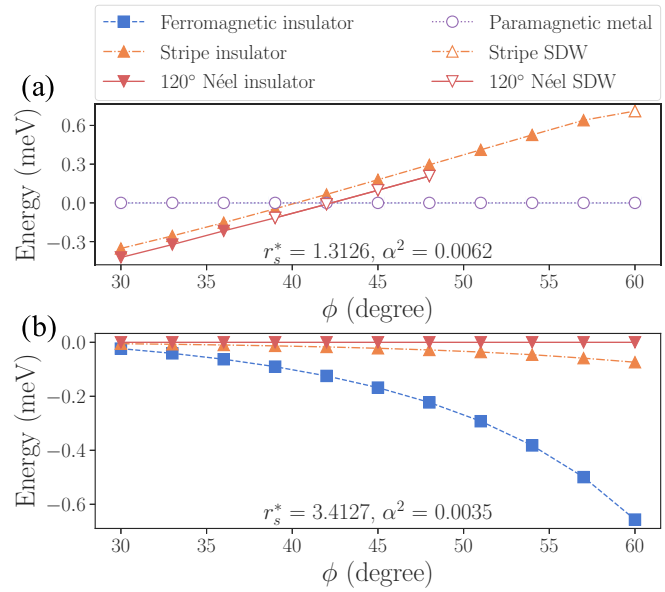

FIG. 6. Mean-field state evolution as a function of the moiré potential phase ϕ. The parameters (r_s^*, α^2) are chosen to be close to (a) the metal-insulator transition and (b) the antiferromagnet-ferromagnet transition at $\phi = 26^\circ$. We change ϕ from 30° (triangular lattice) to 60° (honeycomb lattice). (a) Energy density is plotted relative to the paramagnetic states. An insulator-to-metal transition is observed as we increase ϕ. (b) Energy density is plotted relative to 120° Néel insulators. We do not find any phase transitions in this case.

numbers. The 120° noncollinear states also cannot be topological since they can be continuously tuned, via intermediate umbrella states, to ferromagnetic states without closing the gap between occupied and empty states. More generally, any magnetic insulator that is close to a classical spin state with specific spin orientations on specific sites cannot have a total band Chern number that is nonzero, even if it is not coplanar. The quantum anomalous Hall effect requires itinerancy in this sense. The absence of nontrivial band topology is consistent with the approach used to approximate the phase boundary analytically since only in this case are the Wannier functions exponentially localized, allowing a Gaussian to be a good approximation.

Next, we make a stronger claim, namely, that the intrinsic anomalous Hall conductance is required to be zero even at finite doping whenever the magnetic state is coplanar. One feature of the heterobilayer continuum Hamiltonian, the lack of inversion symmetry except at honeycomb values of ϕ, can lead to ground states with nonzero momentum-space Berry curvature $\Omega(\boldsymbol{k})$ [45], for example, in the 120° Néel state [46]. Because the TRS-breaking 120° state has $\mathcal{T}' \equiv \mathcal{T}\exp(i\pi\mathbf{S}^\perp)$ symmetry, where $\mathbf{S}^\perp$ is the spin operator perpendicular to the 120° ordering plane, it follows that $\Omega(\boldsymbol{k}) = -\Omega(-\boldsymbol{k})$ and that the topological Chern index obtained by integrating the Berry curvature over the Brillouin zone vanishes. It is worth noting that this new composite antiunitary symmetry $\mathcal{T}'$ squares to $+1$ and hence does not imply Kramers degeneracy (see Fig. 2 for band structures). Therefore, $\mathcal{T}'$ is an effective spinless TRS, ensuring that the band structure

satisfies $E_n(k) = E_n(-k)$. This gives the stronger constraint that anomalous Hall conductivity is zero for all doped systems.

While it is certainly possible to measure this nonzero Berry curvature through a nonlinear Hall effect [47], it is hard to distinguish ferromagnetic and 120° orders by this measurement alone since both have the same qualitative Berry curvature properties. We propose an alternate strategy to identify the 120° state that exploits the proximity of noncollinear umbrella [48] states in which all spins are tilted toward the direction of an applied magnetic field [49], breaking $\mathcal{T}'$. Unlike collinear states, coplanar states can evolve into noncoplanar states under a Zeeman field **B**. $\mathcal{T}'$ symmetry can be broken only by a noncoplanar magnetic structure. It is, however, known that coplanar configurations are always favored by quantum fluctuations in an isotropic Heisenberg triangular lattice model system under a Zeeman field [50–52]. Our proposal therefore relies on spin-dependent interactions present in a more accurate continuum model beyond the simplest approximation taken by Eq. (2). If the effective anisotropy is not strong enough to realize the noncoplanar state, the 120° coplanar state can also be measured by its distinctive field-dependent magnetization curve **M**(**B**). Quantum fluctuations favor the collinear up-up-down (UUD) state, among the many competitive coplanar states [50], at a **B** field of around one third the saturation value, where **M**(**B**) shows a wide plateau [48]. These properties motivate future studies aimed at achieving a full understanding of magnetic anisotropies in triangular lattice TMD moiré materials.

IV. DISCUSSION AND OUTLOOK

In this paper we have examined the phase diagram of moiré Hubbard model systems for the special case of half filling of the lowest-energy band. At this filling factor interaction-induced insulating states are normally identified as Mott insulators. The moiré band Hamiltonian [1] depends on the semiconductor effective mass m^*, the moiré potential modulation strength V_M, the moiré lattice constant a_M, and the moiré potential shape parameter ϕ that interpolates between triangular and honeycomb lattice cases. The interaction term is sensitive to screening by polarizable backgrounds (including, but not necessarily limited to [53], screening by the surrounding dielectric), which we characterize collectively by an effective inverse dielectric constant ϵ^{-1}. At fixed band filling, the model parameters can be collapsed to the shape parameter ϕ and two dimensionless coupling constant ratios, r_s^* and α^2, chosen with the goal of minimizing the dependence of the phase diagram on ϕ. r_s^* is the standard electron gas density parameter, and α^2 is proportional to the fraction of the unit cell area occupied by the model's Wannier orbital. We find a phase diagram with two prominent transitions, an expected Mott transition between metallic and insulating states and an unexpected transition between antiferromagnetic and ferromagnetic insulating states. We predict that the metal-insulator transition occurs along a line of nearly constant $U/t_1 \sim 15.1$, where U is the on-site Hubbard interaction and t_1 is the triangular lattice near-neighbor hopping parameter. The value of this ratio on the metal-insulator transition line is comparable to values obtained in numerical studies of simple on-site-interaction triangular lattice Hubbard models [54,55].

The metal-insulator transition line can be crossed by changing the electron density parameter r_s^* by changing the twist angle, by engineering the depth of the modulating moiré potential via a suitable choice of materials, or *in situ* by tuning gate voltages [23,24] or applying pressure [7]. On the insulating side of the metal-insulator transition we find the 120° three-sublattice antiferromagnet expected on triangular lattices with antiferromagnetic interactions between spins. Within the Hartree-Fock approximation, we find a narrow band of intermediate semimetallic states that maintain the 120° semimetallic SDW order of the insulating state. The phase transition between the SDW state and the strongly metallic state is first order.

The SDW phase that appears in our calculations provides one possible explanation for the complex crossover between insulating and metallic states seen in recent experiments [23,24], which hint at an intermediate state with a small, but finite, zero-temperature conductivity [56].

In closing we comment that in this paper we focused on the simplest case in which electronic states are formed from a single microscopic band and therefore described in a continuum model by two-component spinors. In the case of TMD homobilayers [57–60] and in the case of heterobilayers modified by suitably large gate electric fields [61], low-energy bands are present in both layers, yielding low-energy models with four-component spinors that capture both spin and layer degrees of freedom and opening up new opportunities to establish topologically nontrivial states. Indeed, recent heterobilayer experiments [25] found transitions to states with spontaneous valley polarization and anomalous Hall effects in TMDs. We have also limited our attention to one electron per moiré period. Doping away from this limit enriches the physics even more and is thought to lead to superconductivity in some cases. Finally, we have neglected disorder, which might be relevant experimentally, as suggested by the temperature-dependent resistances measured in Ref. [23], which exhibit bumps on the metallic side of the metal-insulator transition similar to the ones seen in Si metal-oxide-semiconductor field-effect transistors [62]. Much remains to be explored in TMD moiré materials.

ACKNOWLEDGMENTS

We acknowledge helpful discussions with N. Morales-Durán, P. Potasz, A. Kumar, and J. Zhu. This work was supported by the U.S. Department of Energy, Office of Science, Basic Energy Sciences, under Award No. DE-SC0019481. The authors acknowledge the Texas Advanced Computing Center (TACC) at The University of Texas at Austin for providing HPC resources that have contributed to the research results reported within this paper.

APPENDIX A: MORE DETAILS ON THE SELF-CONSISTENT HARTREE-FOCK CALCULATIONS

To make the continuum model feasible for a numerical calculation, it is necessary to impose both upper and lower cutoffs in the momentum space. In the atomic-insulator limit,

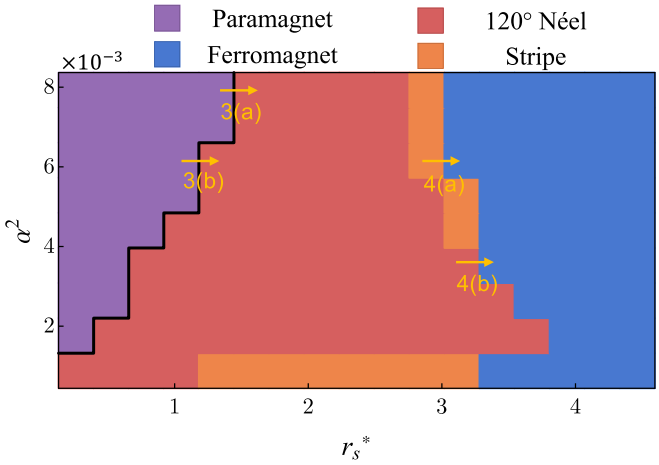

FIG. 7. Pixelated phase diagram for triangular lattice ($\phi = 26°$) moiré materials within the Hartree-Fock approximation.

the real-space Wannier function is well approximated by a Gaussian in a harmonic potential, as argued in the main text. It is then clear that the relevant scale for the upper cutoff can be obtained by comparing the momentum-space Wannier function width with the moiré Brillouin zone size:

$$\frac{1}{a_W}\Big/|\vec{b}| = \sqrt{\frac{m^*\omega}{\hbar}}\Big/|\vec{b}| = \frac{\sqrt{3}}{4\pi}\left(\frac{\beta m^* V_M}{\hbar^2}\right)^{1/4}\sqrt{a_M}. \quad \text{(A1)}$$

That is to say, a larger upper cutoff may be required for stronger interactions. The resulting dimensionless number is of $O(1)$ in our calculation, and we keep the number of momentum shells in the continuum model such that more shells do not change the Hartree-Fock energies up to the convergence accuracy.

As for the lower cutoff, we note that energy density for a periodic system with Coulomb interactions suffers from a finite-size correction, which depends not only on the total number of mesh points N in the moiré Brillouin zone but also on the geometrical detail of the mesh. We correct the finite-size effect by choosing the geometry such that it is compatible with all the pertinent magnetic moiré Brillouin zones and always meshing the moiré Brillouin zone in the same way. In other words, we hold the real-space sample size N fixed for all calculations, which is 108 in our phase diagram calculations. Since the leading finite-size corrections to energy are now state independent, they can be eliminated by evaluating energy differences between states at a fixed system size. We do not actually extrapolate the energies toward the thermodynamic limit since the extrapolation itself incurs further uncertainty.

The actual phase diagram from the self-consistent Hartree-Fock calculation is shown in Fig. 7. Figure 1 in the main text is obtained by fitting the analytical form of the phase boundary to Fig. 7. In the limit of $\alpha \to 0$, we observe different spin configurations converge to the same energy due to the vanishing of the exchange energies J, which we do not show in the main text.

To show the Hartree-Fock band structures in Fig. 2(b) with a clear, small Fermi surface, we increase the system size N to 432. A caveat here is that when we consider a specific magnetic ordered insulating state, the gap size is dependent on the system size because the interaction $U \propto -1/\sqrt{N}$. Hence, there is a slight mismatch in parameters and phases between Figs. 2 and 3. This finite-size correction to the gap size is small when N is large, so the phase boundary of the 120° semimetallic SDW state is still relatively accurate in Fig. 1.

APPENDIX B: PERTURBATIVE EFFECTS OF "NONLOCAL" INTERACTIONS

In this section, we illustrate the induced spin-spin interactions by V_{ah} and V_x in the presence of a large-U Hubbard interaction. For simplicity, we always consider the half-filled case and zero-hopping limit. The ground state lies in the no doubly occupied site sector as in the usual Hubbard model. It can readily be seen that V_{ah} perturbs the ground state out of this sector, so the lowest-order contribution is of order $O(|V_{ah}|^2/U)$. In the spirit of the t/U expansion [41], the leading-order terms are

$$-U^{-1}\sum_{\sigma_1,\sigma_2}\big[\langle 2\sigma_2, 1\bar{\sigma}_2|V_C|1\sigma_2, 1\bar{\sigma}_2\rangle\,\langle 1\sigma_1, 1\bar{\sigma}_1|V_C|1\sigma_1, 2\bar{\sigma}_1\rangle\, c^\dagger_{2\sigma_2}c^\dagger_{1\bar{\sigma}_2}c_{1\bar{\sigma}_2}c_{1\sigma_2}c^\dagger_{1\sigma_1}c^\dagger_{1\bar{\sigma}_1}c_{2\bar{\sigma}_1}c_{1\sigma_1}$$
$$+\langle 1\sigma_2, 2\bar{\sigma}_2|V_C|1\sigma_2, 1\bar{\sigma}_2\rangle\,\langle 1\sigma_1, 1\bar{\sigma}_1|V_C|1\sigma_1, 2\bar{\sigma}_1\rangle\, c^\dagger_{1\sigma_2}c^\dagger_{2\bar{\sigma}_2}c_{1\bar{\sigma}_2}c_{1\sigma_2}c^\dagger_{1\sigma_1}c^\dagger_{1\bar{\sigma}_1}c_{2\bar{\sigma}_1}c_{1\sigma_1}\big] + \text{H.c.}, \quad \text{(B1)}$$

where 1 and 2 label nearest neighbors. The fermionic interactions of the two terms in the square brackets are actually related by a relabeling symmetry: the second term ($\sigma_2 \to \bar{\sigma}_2$) equals the first term. The first term in Eq. (B1) can be simplified, using $\sum_\sigma n_{i\sigma} = 1$, to $-|V_{ah}|^2U^{-1}(-\sum_\sigma c^\dagger_{1\sigma}c_{1\bar{\sigma}}c^\dagger_{2\bar{\sigma}}c_{2\sigma} + \sum_\sigma n_{1\sigma}n_{2\bar{\sigma}}) = -|V_{ah}|^2U^{-1}(1 - \boldsymbol{\sigma}_1\cdot\boldsymbol{\sigma}_2)/2$, where $\boldsymbol{\sigma}_i = c^\dagger_{i\alpha}\boldsymbol{\sigma}_{\alpha\beta}c_{i\beta}$ and $|V_{ah}|^2 = \langle 2, 1|V_C|1, 1\rangle\,\langle 1, 1|V_C|1, 2\rangle$. Hence, it gives rise to the same type of contribution as the normal hopping term in the Hubbard model, i.e., antiferromagnetic coupling.

Now we consider the effects of V_x. V_x actually leaves the number of doubly occupied sites invariant. So the lowest-order contribution is just itself:

$$\sum_{\sigma_1,\sigma_2}\langle 2\sigma_1, 1\sigma_2|V_C|1\sigma_1, 2\sigma_2\rangle\, c^\dagger_{2\sigma_1}c^\dagger_{1\sigma_2}c_{2\sigma_2}c_{1\sigma_1} \quad \text{(B2)}$$
$$= \langle 2, 1|V_C|1, 2\rangle\sum_{\sigma_1,\sigma_2}c^\dagger_{2\sigma_1}c^\dagger_{1\sigma_2}c_{2\sigma_2}c_{1\sigma_1} \quad \text{(B3)}$$
$$= -\frac{\langle 2, 1|V_C|1, 2\rangle}{2}(1 + \boldsymbol{\sigma}_1\cdot\boldsymbol{\sigma}_2), \quad \text{(B4)}$$

which favors the ferromagnetic spin configuration.

[1] F. Wu, T. Lovorn, E. Tutuc, and A. H. MacDonald, Phys. Rev. Lett. **121**, 026402 (2018).

[2] R. Bistritzer and A. H. MacDonald, Proc. Natl. Acad. Sci. USA **108**, 12233 (2011).

[3] E. Suárez Morell, J. D. Correa, P. Vargas, M. Pacheco, and Z. Barticevic, Phys. Rev. B **82**, 121407(R) (2010).

[4] K. Kim, A. DaSilva, S. Huang, B. Fallahazad, S. Larentis, T. Taniguchi, K. Watanabe, B. J. LeRoy, A. H. MacDonald, and E. Tutuc, Proc. Natl. Acad. Sci. USA **114**, 3364 (2017).

[5] Y. Cao, V. Fatemi, A. Demir, S. Fang, S. L. Tomarken, J. Y. Luo, J. D. Sanchez-Yamagishi, K. Watanabe, T. Taniguchi, E. Kaxiras, R. C. Ashoori, and P. Jarillo-Herrero, Nature (London) **556**, 80 (2018).

[6] Y. Cao, V. Fatemi, S. Fang, K. Watanabe, T. Taniguchi, E. Kaxiras, and P. Jarillo-Herrero, Nature (London) **556**, 43 (2018).

[7] M. Yankowitz, S. Chen, H. Polshyn, Y. Zhang, K. Watanabe, T. Taniguchi, D. Graf, A. F. Young, and C. R. Dean, Science **363**, 1059 (2019).

[8] X. Lu, P. Stepanov, W. Yang, M. D. Xie, M. A. Aamir, I. Das, C. Urgell, K. Watanabe, T. Taniguchi, G. Zhang, A. Bachtold, A. H. MacDonald, and D. K. Efetov, Nature (London) **574**, 653 (2019).

[9] A. L. Sharpe, E. J. Fox, A. W. Barnard, J. Finney, K. Watanabe, T. Taniguchi, M. Kastner, and D. Goldhaber-Gordon, Science **365**, 605 (2019).

[10] M. Serlin, C. Tschirhart, H. Polshyn, Y. Zhang, J. Zhu, K. Watanabe, T. Taniguchi, L. Balents, and A. F. Young, Science **367**, 900 (2020).

[11] Y. Cao, D. Rodan-Legrain, O. Rubies-Bigorda, J. M. Park, K. Watanabe, T. Taniguchi, and P. Jarillo-Herrero, Nature (London) **583**, 215 (2020).

[12] C. Shen, Y. Chu, Q. Wu, N. Li, S. Wang, Y. Zhao, J. Tang, J. Liu, J. Tian, K. Watanabe, T. Taniguchi, R. Yang, Z. Y. Meng, and D. Shi, O. V. Yazyev, and G. Zhang, Nat. Phys. **16**, 520 (2020).

[13] G. Chen, L. Jiang, S. Wu, B. Lyu, H. Li, B. L. Chittari, K. Watanabe, T. Taniguchi, Z. Shi, J. Jung, Y. Zhang, and F. Wang, Nat. Phys. **15**, 237 (2019).

[14] G. Chen, A. L. Sharpe, P. Gallagher, I. T. Rosen, E. J. Fox, L. Jiang, B. Lyu, H. Li, K. Watanabe, T. Taniguchi, J. Jung, Z. Shi, D. Goldhaber-Gordon, Y. Zhang, and F. Wang, Nature (London) **572**, 215 (2019).

[15] Y. Tang, L. Li, T. Li, Y. Xu, S. Liu, K. Barmak, K. Watanabe, T. Taniguchi, A. H. MacDonald, J. Shan, and K. F. Mak, Nature (London) **579**, 353 (2020).

[16] E. C. Regan, D. Wang, C. Jin, M. I. B. Utama, B. Gao, X. Wei, S. Zhao, W. Zhao, Z. Zhang, K. Yumigeta, M. Blei, J. D. Carlström, K. Watanabe, T. Taniguchi, S. Tongay, M. F. Crommie, A. Zettl, and F. Wang, Nature (London) **579**, 359 (2020).

[17] L. Wang, E.-M. Shih, A. Ghiotto, L. Xian, D. A. Rhodes, C. Tan, M. Claassen, D. M. Kennes, Y. Bai, B. Kim, K. Watanabe, T. Taniguchi, X. Zhu, J. C. Hone, A. Rubio, A. N. Pasupathy, and C. R. Dean, Nat. Mater. **19**, 861 (2020).

[18] Y. Xu, S. Liu, D. A. Rhodes, K. Watanabe, T. Taniguchi, J. Hone, V. Elser, K. F. Mak, and J. Shan, Nature (London) **587**, 214 (2020).

[19] C. Jin, Z. Tao, T. Li, Y. Xu, Y. Tang, J. Zhu, S. Liu, K. Watanabe, T. Taniguchi, J. C. Hone, L. Fu, J. Shan, and K. F. Mak, Nat. Mater. **20**, 940 (2021).

[20] T. Li, J. Zhu, Y. Tang, K. Watanabe, T. Taniguchi, V. Elser, J. Shan, and K. F. Mak, Nat. Nanotechnol. **16**, 1068 (2021).

[21] H. Li, S. Li, M. H. Naik, J. Xie, X. Li, E. C. Regan, D. Wang, W. Zhao, K. Yumigeta, M. Blei, T. Taniguchi, K. Watanabe, S. Tongay, A. Zettl, S. G. Louie, M. F. Crommie, and F. Wang, Nat. Phys. **17**, 1114 (2021).

[22] X. Huang, T. Wang, S. Miao, C. Wang, Z. Li, Z. Lian, T. Taniguchi, K. Watanabe, S. Okamoto, D. Xiao, S.-F. Shi, and Y.-T. Cui, Nat. Phys. **17**, 715 (2021).

[23] T. Li, S. Jiang, L. Li, Y. Zhang, K. Kang, J. Zhu, K. Watanabe, T. Taniguchi, D. Chowdhury, L. Fu, J. Shan, and K. F. Mak, Nature **597**, 350 (2021).

[24] A. Ghiotto, E.-M. Shih, G. Pereira, D. A. Rhodes, B. Kim, J. Zang, A. J. Millis, K. Watanabe, T. Taniguchi, J. C. Hone, L. Wang, C. R. Dean, and A. N. Pasupathy, Nature **597**, 345 (2021).

[25] T. Li, S. Jiang, B. Shen, Y. Zhang, L. Li, T. Devakul, K. Watanabe, T. Taniguchi, L. Fu, J. Shan, and K. F. Mak, arXiv:2107.01796.

[26] M. Angeli and A. H. MacDonald, Proc. Natl. Acad. Sci. USA **118**, e2021826118 (2021).

[27] Y. Zhang, N. F. Q. Yuan, and L. Fu, Phys. Rev. B **102**, 201115(R) (2020).

[28] J. P. Perdew and A. Zunger, Phys. Rev. B **23**, 5048 (1981).

[29] N. Morales-Durán, A. H. MacDonald, and P. Potasz, Phys. Rev. B **103**, L241110 (2021).

[30] T. Jolicoeur, E. Dagotto, E. Gagliano, and S. Bacci, Phys. Rev. B **42**, 4800 (1990).

[31] F. Wu, T. Lovorn, and A. H. MacDonald, Phys. Rev. Lett. **118**, 147401 (2017).

[32] This choice of β ensures that the harmonic expansion is performed around the global minimum of the modulation potential. The properties of TMD moiré materials are invariant under $\phi \to -\phi$ and $\phi \to \phi + k120^\circ$.

[33] B. Tanatar and D. M. Ceperley, Phys. Rev. B **39**, 5005 (1989).

[34] C. Attaccalite, S. Moroni, P. Gori-Giorgi, and G. B. Bachelet, Phys. Rev. Lett. **88**, 256601 (2002).

[35] R. Kaneko, S. Morita, and M. Imada, J. Phys. Soc. Jpn. **83**, 093707 (2014).

[36] Z. Zhu and S. R. White, Phys. Rev. B **92**, 041105(R) (2015).

[37] W.-J. Hu, S.-S. Gong, W. Zhu, and D. N. Sheng, Phys. Rev. B **92**, 140403(R) (2015).

[38] Y. Iqbal, W.-J. Hu, R. Thomale, D. Poilblanc, and F. Becca, Phys. Rev. B **93**, 144411 (2016).

[39] S.-S. Gong, W. Zhu, J.-X. Zhu, D. N. Sheng, and K. Yang, Phys. Rev. B **96**, 075116 (2017).

[40] Z. Zhu, P. A. Maksimov, S. R. White, and A. L. Chernyshev, Phys. Rev. Lett. **120**, 207203 (2018).

[41] A. H. MacDonald, S. M. Girvin, and D. Yoshioka, Phys. Rev. B **37**, 9753 (1988).

[42] N. Morales-Durán, N. C. Hu, P. Potasz, and A. H. MacDonald, arXiv:2108.03313.

[43] See Appendix B for a more formal explanation via an expansion around the flat-band limit.

[44] Increasing α^2, the parameter that measures the relative spread of the Wannier functions, increases both t_1 and $|V_x|$. From Eqs. (13) and (21) we see that $|V_x|$ increases more rapidly than t_1^2. This explains why $\alpha^2 \sim 1/r_s^*$ along the ferromagnetic-antiferromagnetic phase boundary.
[45] D. Xiao, M.-C. Chang, and Q. Niu, Rev. Mod. Phys. **82**, 1959 (2010).
[46] H. Chen, Q. Niu, and A. H. MacDonald, Phys. Rev. Lett. **112**, 017205 (2014).
[47] I. Sodemann and L. Fu, Phys. Rev. Lett. **115**, 216806 (2015).
[48] O. A. Starykh, Rep. Prog. Phys. **78**, 052502 (2015).
[49] To a good approximation, only the out-of-plane spin component couples to the magnetic field in a K-valley heterobilayer system due to strong spin-orbit coupling. However, we estimate that the leading-order orbital effect, the three-spin chiral interaction, from the out-of-plane field is small away from the metal-insulator phase boundary. This complication is absent in the Γ-valley systems [26].
[50] M. Ye and A. V. Chubukov, Phys. Rev. B **95**, 014425 (2017).
[51] D. Farnell, R. Bishop, and J. Richter, J. Stat. Phys. **176**, 180 (2019).
[52] A. L. Chernyshev and O. A. Starykh, arXiv:2109.10916.
[53] X. Liu, Z. Wang, K. Watanabe, T. Taniguchi, O. Vafek, and J. Li, Science **371**, 1261 (2021).
[54] A. Szasz, J. Motruk, M. P. Zaletel, and J. E. Moore, Phys. Rev. X **10**, 021042 (2020).
[55] L. F. Tocchio, A. Montorsi, and F. Becca, Phys. Rev. B **102**, 115150 (2020).
[56] A resistance jump also occurs at the critical point in electron-fractionalization [63,64] metal-insulator transition scenarios but for completely different reasons.
[57] F. Wu, T. Lovorn, E. Tutuc, I. Martin, and A. H. MacDonald, Phys. Rev. Lett. **122**, 086402 (2019).
[58] H. Pan, F. Wu, and S. Das Sarma, Phys. Rev. Research **2**, 033087 (2020).
[59] J. Zang, J. Wang, J. Cano, and A. J. Millis, Phys. Rev. B **104**, 075150 (2021).
[60] T. Devakul, V. Crépel, Y. Zhang, and L. Fu, Nature Commun. **12**, 6730 (2021).
[61] Y. Zhang, T. Devakul, and L. Fu, Proc. Natl. Acad. Sci. USA **118**, e2112673118 (2021).
[62] A. Punnoose and A. M. Finkel'stein, Phys. Rev. Lett. **88**, 016802 (2001).
[63] T. Senthil, Phys. Rev. B **78**, 045109 (2008).
[64] Y. Xu, Z.-X. Luo, C.-M. Jian, and C. Xu, arXiv:2106.14910.